

DOI 10.24425/aee.2021.136052

## Subsynchronous oscillation and its mitigation of VSC-MTDC with doubly-fed induction generator-based wind farm integration

MIAOHONG SU<sup>1</sup> , HAIYING DONG<sup>1,2</sup>, KAIQI LIU<sup>1</sup>, WEIWEI ZOU<sup>1</sup><sup>1</sup>*School of Automatic and Electrical Engineering, Lanzhou Jiaotong University  
China*<sup>2</sup>*School of New Energy and Power Engineering, Lanzhou Jiaotong University  
China**e-mails: [hydong@mail.lzjtu.cn](mailto:hydong@mail.lzjtu.cn), [sumiaohong9@163.com](mailto:sumiaohong9@163.com)*

(Received: 26.04.2020, revised: 09.08.2020)

**Abstract:** Wind power integration through the voltage source converter-based high-voltage direct current (VSC-HVDC) system will be a potential solution for delivering large-scale wind power to the “Three-North Regions” of China. However, the interaction between the doubly-fed induction generator (DFIG) and VSC-HVDC system may cause the risk of subsynchronous oscillation (SSO). This paper establishes a small-signal model of the VSC based multi-terminal direct current (VSC-MTDC) system with new energy access for the problem, and the influencing factors causing SSO are analyzed based on the eigenvalue analysis method. The theoretical analysis results show that the SSO in the system is related to the wind farm operating conditions, the rotor-side controller (RSC) of the DFIG and the interaction of the controller in the VSC-MTDC system. Then, the phase lag characteristic is obtained based on the signal test method, and a multi-channel variable-parameter subsynchronous damping controller (SSDC) is designed via selecting reasonable parameters. Finally, the correctness of the theoretical analysis and the effectiveness of the multi-channel variable-parameter SSDC are verified based on time-domain simulation.

**Key words:** doubly-fed induction generator, eigenvalue analysis, multi-channel variable-parameter subsynchronous damping controller, subsynchronous oscillation voltage source converter based multi-terminal direct current transmission system



© 2021. The Author(s). This is an open-access article distributed under the terms of the Creative Commons Attribution-NonCommercial-NoDerivatives License (CC BY-NC-ND 4.0, <https://creativecommons.org/licenses/by-nc-nd/4.0/>), which permits use, distribution, and reproduction in any medium, provided that the Article is properly cited, the use is non-commercial, and no modifications or adaptations are made.

## 1. Introduction

It is urgent to carry out long-distance transmission of wind power because wind resources and power demand are inversely distributed in the “Three-North Regions” of China [1]. Compared with the voltage source converter-based high-voltage direct current (VSC-HVDC) system, VSC-based multi-terminal direct current (VSC-MTDC) not only can solve the problem, but also has the advantages such as economy, flexibility and reliability, it has more technical advantages and can better ensure the reliable output of a wind farm [1–4]. However, with the access of large-scale wind power, the interaction mechanism between a wind turbine and VSC-MTDC control device is more complicated and may cause subsynchronous oscillation (SSO). Therefore, the safe and stable operation of the power grid faces greater challenges [5–9].

Regarding SSO problems caused by wind power, the existing research is based on a simple grid-connected model of the direct-drive permanent magnet synchronous generator (D-PMSG) or the doubly-fed induction generator (DFIG). There are few studies that have studied the SSO of the DFIG delivered by the VSC-MTDC. In [10, 11], the stability of the system of a DFIG-based wind farm via the VSC-HVDC grid-connected system is studied, but there is no oscillation mode due to interaction. In [12, 13], it is found that the improper matching of VSC-HVDC and DFIG control parameters would cause SSO. In [14], two types of SSO induced by the grid connection of offshore wind farms via VSC-HVDC are studied, and the coordinated suppression measures are proposed. In [15, 16], the SSO caused by a DFIG-based wind farm connected to the grid by the modular multilevel converter-based HVDC (MMC-HVDC) is studied, and the control strategy of additional SSO current suppression is proposed. In [17, 18], the SSO and multi-band oscillations caused by a D-PMSG-based wind farm connected to the grid via the VSC-HVDC are studied. Besides, additional damping controllers on the machine and grid sides are designed [18]. In [19], the SSO characteristics of a D-PMSG-based wind farm connected to the grid via the MMC-HVDC are studied, and the SSO is suppressed via adding a series virtual resistor to the MMC outer loop controller.

In summary, most of the existing researches have studied the SSO mechanism and suppression method of wind power via VSC-HVDC grid connection. However, the VSC-MTDC system is more complex, and because of the randomness and fluctuation of wind power, the suppression methods mentioned above have low adaptability of operating conditions. Therefore, the paper takes the SSO caused by the interaction between the DFIG-based wind farm and VSC-MTDC system as the research object. The authors established a small-signal model of the whole system and analyze the SSO characteristics based on the eigenvalue analysis method. A multi-channel subsynchronous damping controller (SSDC) is designed based on the principle of the power system stabilizer (PSS) to suppress low frequency oscillation. Finally, the correctness of the theoretical analysis and the effectiveness of the suppression method are verified.

## 2. System modeling

Fig. 1 shows the structure of a DFIG-based wind farm integrated with the grid via the VSC-MTDC system. The DFIG adopts the form of “one machine and one transformer”. A single wind turbine is connected to a 35 kV collector line via a generator-side transformer, and then connected

to the VSC-MTDC system via 35/330/750 kV transformers. The paper ignores the interaction between wind turbines. Therefore, the wind farm can be equivalent to a single wind turbine.

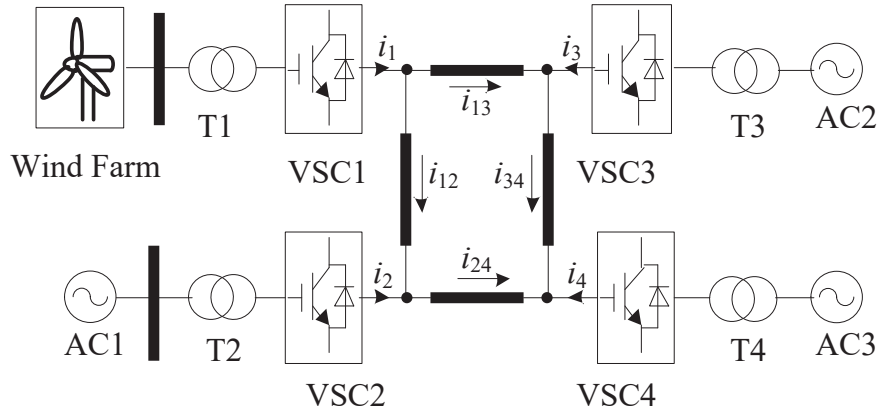


Fig. 1. Structure diagram of VSC-MTDC for DFIG-based wind farm

In Fig. 1, VSC1 provides stable AC power for the point of common coupling (PCC) and controls the amplitude and frequency of AC voltage. VSC3 uses constant DC voltage control and provides voltage support for the DC system. VSC2 and VSC4 use active power control.

## 2.1. Modeling of DFIG power generation system

1) A mathematical model of a wind turbine shaft

The two-mass model of a wind turbine shaft can be described as [20,21]:

$$\begin{cases} 2H_t \frac{d\omega_t}{dt} = T_m - K_s \theta_s - B_s \frac{d\theta_s}{dt} \\ 2H_g \frac{d\omega_r}{dt} = -T_s + K_s \theta_s + B_s \frac{d\theta_s}{dt} \\ \frac{d\theta_s}{dt} = \omega_t - \omega_r, \quad \frac{d\theta_r}{dt} = \omega_r \end{cases}, \quad (1)$$

where:  $H_t$  is the inertia constant of the wind turbine mass,  $\omega_t$  is the wind turbine speed,  $T_m$  is the mechanical torque of the wind turbine,  $K_s$  is the stiffness coefficient of the transmission shaft,  $\theta_s$  is the torsional vibration angle of the shafting,  $B_s$  is the torsional vibration damping coefficient of the transmission shaft,  $H_g$  is the inertia constant of the mass of the generator,  $\omega_r$  is the angular velocity of the rotor,  $T_e$  is the electromagnetic torque of the induction motor.

Linearize (1) and the small-signal model of the shafting can be obtained as shown in (2).

$$\Delta \dot{\mathbf{x}}_M = \mathbf{A}_M \Delta \mathbf{x}_M + \mathbf{B}_M \Delta \mathbf{u}_M, \quad \Delta \mathbf{y}_M = \mathbf{C}_M \Delta \mathbf{x}_M + \mathbf{D}_M \Delta \mathbf{u}_M, \quad (2)$$

where:

$$\Delta \mathbf{x}_M = [\Delta \omega_r, \Delta \omega, \Delta \theta_r, \Delta \theta_s]^T, \quad \Delta \mathbf{u}_M = [\Delta T_m, \Delta T_e]^T.$$

## 2) A mathematical model of an induction generator

It is modeled in a  $dq$  synchronous rotating coordinate system. Both stator side and rotor side use the motor convention and parameters of the rotor side are convert to the stator side [20,21].

$$\begin{cases} u_{ds} = R_s i_{ds} - \omega_s \psi_{qs} + \frac{1}{\omega_s} \frac{d\psi_{ds}}{dt}, & u_{qs} = R_s i_{qs} - \omega_s \psi_{ds} + \frac{1}{\omega_b} \frac{d\psi_{qs}}{dt} \\ u_{dr} = R_r i_{dr} - (\omega_s - \omega_r) \psi_{qr} + \frac{1}{\omega_b} \frac{d\psi_{dr}}{dt}, & u_{qr} = R_r i_{qr} - (\omega_s - \omega_r) \psi_{dr} + \frac{1}{\omega_b} \frac{d\psi_{qr}}{dt} \\ \psi_{qs} = (X_s + X_m) i_{qs} + X_m i_{qr}, & \psi_{ds} = (X_s + X_m) i_{ds} + X_m i_{dr} \\ \psi_{qr} = (X_r + X_m) i_{qr} + X_m i_{qs}, & \psi_{dr} = (X_r + X_m) i_{dr} + X_m i_{ds} \end{cases} \quad (3)$$

where: the subscripts  $s$  and  $r$  represent the stator and rotor, respectively; the subscripts  $d$  and  $q$  represent the  $d$ -axis component and  $q$ -axis component, respectively;  $\Delta\psi$  is the flux linkage;  $R$  represents resistances of the  $dq$  axis of the stator and rotor;  $\omega_s$  is the angular velocity of the stator, that is, the rotational speed of the synchronous rotating coordinate system;  $\omega_b$  is the system reference frequency;  $X_s$ ,  $X_r$ , and  $X_m$  stand for the stator and rotor winding reactance, respectively.

The small-signal model of the induction generator can be obtained by linearizing (3).

$$\Delta \dot{\mathbf{x}}_G = \mathbf{A}_G \Delta \mathbf{x}_G + \mathbf{B}_G \Delta \mathbf{u}_G, \quad \Delta \mathbf{y}_G = \mathbf{C}_G \Delta \mathbf{x}_G + \mathbf{D}_G \Delta \mathbf{u}_G, \quad (4)$$

where:  $\Delta \mathbf{x}_G = [\Delta\psi_{qs}, \Delta\psi_{ds}, \Delta\psi_{qr}, \Delta\psi_{dr}]^T$ ,  $\Delta \mathbf{u}_G = [\Delta u_{qs}, \Delta u_{ds}, \Delta u_{qr}, \Delta u_{dr}, \Delta \omega_r]^T$ .

## 3) A mathematical model of a rotor side converter

The stator voltage orientated control (SVOC) is used in the rotor side converter (RSC). The stator voltage vector orientation usually coincides with the  $d$ -axis of the synchronous rotating coordinate system. Therefore,  $u_{ds} = U_s = -\omega_s \psi_{qs}$ ,  $u_{qs} = 0$ , and the following can be obtained:

$$\psi_{ds} = 0, \quad \psi_{qs} = \psi_s = -\frac{U_s}{\omega_s}, \quad i_{ds} = -\frac{L_m}{L_{ss}} i_{dr}, \quad i_{qs} = -\frac{1}{L_{ss}} \left( \frac{U_s}{\omega_s} + L_m i_{qr} \right), \quad (5)$$

where:  $U_s$  is the magnitude of the stator voltage vector.  $L_{ss}$  is the stator self-induction coefficient in the  $dq$  system.  $L_m$  is the mutual inductance between the stator and rotor in the  $dq$  coordinate system.

Therefore, the active and reactive power of the stator can be obtained:

$$\begin{aligned} P_s &= \frac{3}{2} (u_{ds} i_{ds} + u_{qs} i_{qs}) = \frac{3L_m}{2L_{ss}} U_s i_{dr}, \\ Q_s &= \frac{3}{2} (u_{qs} i_{ds} - u_{ds} i_{qs}) = -\frac{3U_s}{2\omega_1 L_{ss}} (U_s + \omega_s L_m i_{qr}). \end{aligned} \quad (6)$$

The voltage of the rotor is as follows:

$$\begin{aligned} u_{dr} &= R_r i_{dr} + \sigma L_{rr} \frac{di_{dr}}{dt} - \omega_{\text{slip}} \left( -\frac{L_m}{\omega_s L_{ss}} U_s + \sigma L_{rr} i_{qr} \right), \\ u_{qr} &= R_r i_{qr} + \sigma L_{rr} \frac{di_{qr}}{dt} + \omega_{\text{slip}} \sigma L_{rr} i_{qr}, \end{aligned} \quad (7)$$

where:  $\omega_{\text{slip}} = \omega_s - \omega_r$ ,  $\omega_s = 2\pi f_s$ ,  $f_s$  is the frequency of the stator,  $L_{rr}$  is the rotor self-induction coefficient in the  $dq$  coordinate system,  $\sigma$  is the magnetic flux leakage coefficient of the generator.

In summary, the control block diagram of the RSC is shown in Fig. 2. Fig. 2 shows that  $K_{P1}$ ,  $K_{I1}$ ,  $K_{P3}$ , and  $K_{I3}$  are the proportional and integral gains of the RSC outer loop,  $P_{s\text{ref}}$  and  $Q_{s\text{ref}}$  are the reference values of the stator active and reactive power,  $K_{P2}$  and  $K_{I2}$  are the proportional and integral gains of the RSC inner loop.

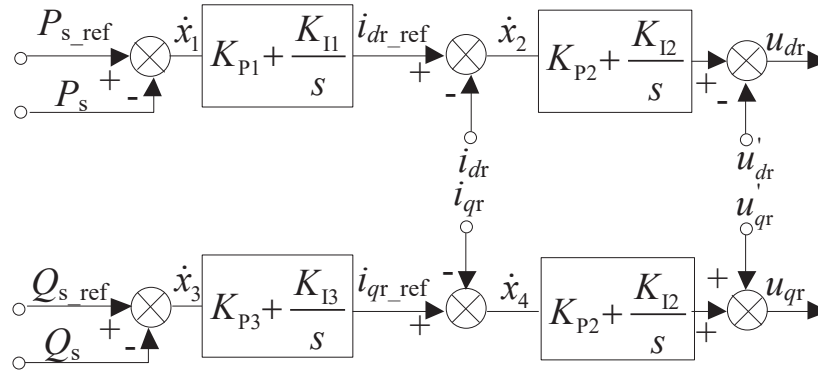


Fig. 2. Control block diagram of RSC

Therefore, the small-signal model of the RSC can be obtained.

$$\Delta \dot{\mathbf{x}}_r = \mathbf{A}_r \Delta \mathbf{x}_r + \mathbf{B}_r \Delta \mathbf{u}_r, \quad \Delta \mathbf{y}_r = \mathbf{C}_r \Delta \mathbf{x}_r + \mathbf{D}_r \Delta \mathbf{u}_r, \quad (8)$$

where:  $\Delta \mathbf{x}_r = [\Delta x_1, \Delta x_2, \Delta x_3, \Delta x_4]^T$ ,  $\Delta \mathbf{u}_r = [\Delta u_{ds}, \Delta u_{qs}, \Delta i_{ds}, \Delta i_{qs}, \Delta i_{dr}, \Delta i_{qr}, \Delta P_{s\text{ref}}, \Delta Q_{s\text{ref}}]^T$ .

4) A mathematical model of a grid side converter

The SVOC is adopted in the grid side converter (GSC), which is operating in unity power factor mode. The mathematical model of the GSC in the  $dq$  synchronous coordinate system is as follows:

$$\begin{cases} u_{dg} = -R_g i_{dg} - L_g \frac{di_{dg}}{dt} + \omega_s L_g i_{qg} + u_{ds}, & u_{qg} = -R_g i_{qg} - L_g \frac{di_{qg}}{dt} - \omega_s L_g i_{dg} + u_{qs} \\ \frac{dU_{dc}}{dt} = \frac{i_{cg} - i_{cr}}{C_{dc0}} \end{cases}, \quad (9)$$

where:  $u_{dg}$  and  $u_{qg}$  are the converter arm side voltage components of the  $d$ -axis and  $q$ -axis,  $i_{dg}$  and  $i_{qg}$  are the converter input current components of the  $d$ -axis and  $q$ -axis,  $L_g$  and  $R_g$  are the inductor and resistance on the converter side,  $C_{dc0}$  is the DC bus voltage of the back-to-back converters,  $U_{dc}$  is the capacitor voltage of the DC bus,  $i_{cg}$  is the current flowing from the GSC to the DC bus, and  $i_{cr}$  is the current flowing from the DC bus to the RSC.

It can be seen from (9) that  $u_{dg}$  and  $u_{qg}$  on the bridge arm side are affected by the cross-coupling and grid voltage disturbance terms, respectively. Since the GSC also uses the SVOC, the amount of disturbance can be abbreviated as:

$$u'_{dg} = \omega_s L_g i_{qg} + U_{ds}, \quad u'_{qg} = -\omega_s L_g i_{dg}.$$

In summary, the control block diagram of the GSC is shown in Fig. 3.

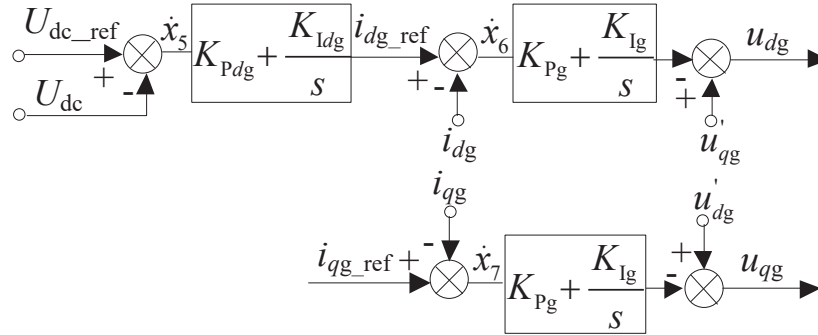


Fig. 3. Control block diagram of GSC

where:  $K_{Pg}$  and  $K_{Ig}$  are the proportional and integral gains of the GSC inner loop,  $U_{dc\text{ref}}$  is the reference value of  $U_{dc}$ ,  $K_{Pdg}$  and  $K_{Idg}$  are the proportional and integral gains of the GSC outer loop.

Therefore, the small-signal model of the GSC can be obtained.

$$\Delta \dot{\mathbf{x}}_g = \mathbf{A}_g \Delta \mathbf{x}_g + \mathbf{B}_g \Delta \mathbf{u}_g, \quad \Delta \mathbf{y}_g = \mathbf{C}_g \Delta \mathbf{x}_g + \mathbf{D}_g \Delta \mathbf{u}_g, \quad (10)$$

where:

$$\Delta \mathbf{x}_g = [\Delta x_5, \Delta x_6, \Delta x_7]^T, \quad \Delta \mathbf{u}_g = [\Delta U_{DC\text{ref}}, \Delta U_{DC}, \Delta i_{qg\text{ref}}, \Delta i_{dg}, \Delta i_{qg}]^T.$$

## 2.2. Modeling of VSC-MTDC system

According to the modular modeling method in [22], the small-signal model of each subsystem can be obtained.

The small-signal model of AC and DC sides of VSC1 are as shown in (11) and (12).

$$\Delta \dot{\mathbf{x}}_{ac} = \mathbf{A}_{ac} \Delta \mathbf{x}_{ac} + \mathbf{B}_{ac} \Delta \mathbf{u}_{ac}, \quad (11)$$

where:

$$\Delta \mathbf{x}_{ac} = [\Delta i_d, \Delta i_q]^T, \quad \Delta \mathbf{u}_{ac} = [\Delta u_{cd}, \Delta u_{cq}, \Delta u_{sd}, \Delta u_{sq}]^T.$$

$$\Delta \dot{\mathbf{x}}_{dc} = \mathbf{A}_{dc} \Delta \mathbf{x}_{dc} + \mathbf{B}_{dc} \Delta \mathbf{u}_{dc}, \quad (12)$$

where:

$$\Delta \mathbf{x}_{dc} = [\Delta i_{dc1}]^T, \quad \Delta \mathbf{u}_{dc} = [\Delta i_{line}].$$

VSCs of the VSC-MTDC system mostly adopt double closed loop control [23,24], the control block diagram of which is shown in Fig. 4.

In Fig. 4,  $K_{PO}$  and  $K_{IO}$  are the proportional and integral gains of the outer loop controller.  $K_{PI}$  and  $K_{II}$  are the proportional and integral gains of the inner loop controller.  $L_1$  is the equivalent inductance for the coupling reactor and transformer.

The small-signal model of VSC1 can be obtained by combining the control block diagram shown in Fig. 4 with the control strategy described in Section 2.

$$\Delta \dot{\mathbf{x}}_c = \mathbf{A}_c \Delta \mathbf{x}_c + \mathbf{B}_c \Delta \mathbf{u}_c, \quad \Delta \mathbf{y}_c = \mathbf{C}_c \Delta \mathbf{x}_c + \mathbf{D}_c \Delta \mathbf{u}_c, \quad (13)$$

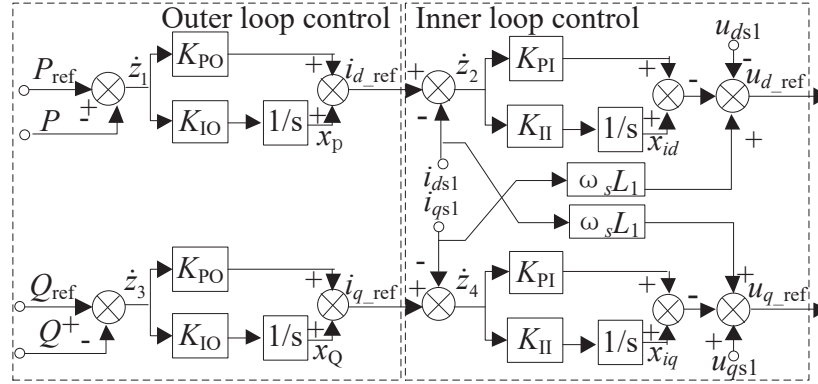


Fig. 4. Control block diagram of active and reactive power controller

where:

$$\Delta \mathbf{x}_c = [\Delta z_1, \Delta z_2, \Delta z_3, \Delta z_4]^T, \quad \Delta \mathbf{u}_c = [\Delta u_{ac}, \Delta u_{ac\_ref}, \Delta f, \Delta f_{ref}]^T.$$

In order to simplify the modeling of VSCs, the flags can be added to the control block diagram of the VSC [22]. Therefore, the small-signal models of VSC2~VSC4 controllers can be derived.

The control block diagram of the phase lock loop (PLL) can be obtained from [22], and the small-signal model of the PLL can be obtained, which is shown in (14).

$$\Delta \dot{\mathbf{x}}_{pll} = \mathbf{A}_{pll} \Delta \mathbf{x}_{pll} + \mathbf{B}_{pll} \Delta \mathbf{u}_{pll}, \quad \Delta \theta = \mathbf{C}_{pll} \Delta \mathbf{x}_{pll}, \quad (14)$$

where:

$$\Delta \mathbf{x}_{pll} = [\Delta x_{pll}, \Delta \theta]^T, \quad \Delta \mathbf{u}_{pll} = [\Delta \varphi],$$

$\varphi$  is the voltage phase at the PCC point,  $\theta$  is the output of the PLL.

In summary, the small-signal model of the VSC-MTDC system can be obtained.

$$\Delta \dot{\mathbf{x}}_{sys} = \mathbf{A}_{sys} \Delta \mathbf{x}_{sys} + \mathbf{B}_{sys} \Delta \mathbf{u}_{sys}, \quad (15)$$

where:

$$\Delta \mathbf{x}_{sys} = [\Delta \mathbf{x}_{con1}, \Delta \mathbf{x}_{con2}, \Delta \mathbf{x}_{con3}, \Delta \mathbf{x}_{con4}, \Delta \mathbf{x}_{net}]^T, \quad \Delta \mathbf{x}_{con_i} = [\Delta \mathbf{x}_{ac_i}, \Delta \mathbf{x}_{dc_i}, \Delta \mathbf{x}_{c_i}, \Delta \mathbf{x}_{pll_i}]^T,$$

$i$  represents a different VSC,  $\Delta \mathbf{x}_{net}$  is the state vector of the DC transmission line.

### 2.3. Small-signal model of the whole system

According to the above derivation, the small-signal model of the whole system can be obtained.

$$\Delta \dot{\mathbf{x}} = \mathbf{A} \Delta \mathbf{x} + \mathbf{B} \Delta \mathbf{u}, \quad (16)$$

where:  $\Delta \mathbf{x}$  is the state vector,  $\Delta \mathbf{u}$  is the input vector,  $\mathbf{A}$  is the state matrix,  $\mathbf{B}$  is the input matrix.  $\Delta \mathbf{x}$  is composed of the state vector  $\Delta \mathbf{x}_{DFIG}$  of the DFIG and the state vector  $\Delta \mathbf{x}_{sys}$  of the VSC-MTDC system, where:

$$\Delta \mathbf{x}_{DFIG} = [\Delta \omega_r, \Delta \omega_t, \Delta \theta_r, \Delta \theta_s, \Delta \psi_{qs}, \Delta \psi_{ds}, \Delta \psi_{qr}, \Delta \psi_{dr}, \Delta U_{DC}, \Delta x_1, \Delta x_2, \Delta x_3, \Delta x_4, \Delta x_5, \Delta x_6, \Delta x_7]^T,$$

$$\Delta \mathbf{x}_{sys} = [\Delta \mathbf{X}_{con1}, \Delta \mathbf{X}_{con2}, \Delta \mathbf{X}_{con3}, \Delta \mathbf{X}_{con4}, \Delta \mathbf{X}_{net}]^T.$$

### 3. SSO characteristics analysis of the system

Based on the small-signal model of the whole system established above, the eigenvalue analysis method is used to analyze the SSO characteristics.

#### 3.1. Eigenvalue analysis of the system

The set capacity of the wind farm is 500 MW, the wind speed and the rotate speed are 8.5 m/s and 0.8 pu, the rated rotor speed is 1.2 pu. Some parameters of the system are shown in Table 1.

Table 1. Parameters of the system

Parameters	Value
Output voltage of DFIG/kV	0.69
Rated wind speed/(m/s)	12
Rated DC voltage of VSC/kV	800
Rated Capacity of VSC1/MW	500
Proportional/integral coefficient ( $K_{PO1}/K_{IO1}$ ) of outer loop controller of VSC1	0.8/10
Proportional/integral coefficient ( $K_{PI1}/K_{II1}$ ) of Inner loop controller of VSC1	0.5/10
Proportional/integral coefficient ( $K_{PPLL VSC1}/K_{IPLL VSC1}$ ) of PLL of VSC1	2/200

Therefore, 13 pairs of SSO modes which are shown in Table 2 can be obtained when the system runs stably and the oscillation modes in the high frequency band are ignored.

Table 2. Main oscillation modes

Modes	$\delta \pm j \omega$	f/Hz	Damping ratio	Modes	$\delta \pm j \omega$	f/Hz	Damping ratio
1	$-13.1 \pm j313.00$	49.97	0.042	8	$-5.72 \pm j174.05$	27.70	0.033
2	$-28.05 \pm j188.28$	29.97	0.147	9	$-1.86 \pm j324.52$	27.39	0.011
3	$-4.98 \pm j69.18$	11.01	0.072	10	$-16.51 \pm j20.46$	3.27	0.628
4	$-0.83 \pm j142.38$	22.66	0.006	11	$-10.00 \pm j22.36$	3.56	0.408
5	$-0.99 \pm j22.72$	3.62	0.044	12	$-1.16 \pm j13.98$	2.22	0.083
6	$-12.91 \pm j217.04$	34.54	0.059	13	$-0.86 \pm j14.20$	2.26	0.060
7	$-4.31 \pm j217.03$	34.54	0.020				

The following conclusions can be obtained via the participation factor analysis. Mode 1, Mode 2 and Mode 4 are related to the magnetic link of the stator and rotor of the DFIG. Besides, Mode 4 is also related to the RSC and the control mode of VSC1. Mode 3 is related to the RSC. Mode 5 is related to the control of VSC1 and VSC2. Mode 6 and Mode 7 are related to the control of VSC3. Mode 8 is related to the control of VSC1 and VSC3. Mode 9 is related to the control of VSC1. Mode 10 is related to the control of VSC3 and VSC4. Mode 11 is related to the control of

VSC2 and VSC4. Mode 12 is related to the control of VSC2 and VSC3. Mode 13 is related to DC transmission lines. From Table 2 we can see that there is no interaction with the state variables on the VSC-MTDC system in the modes dominated by the DFIG. The modes dominated by the VSC-MTDC system are all related to its PI parameters. While the damping ratio is the lowest when SSO is caused via the control interaction of the DFIG and VSC1. Therefore, the detailed participation factor analysis of Mode 4 (SSO-4) is shown in Fig. 5.

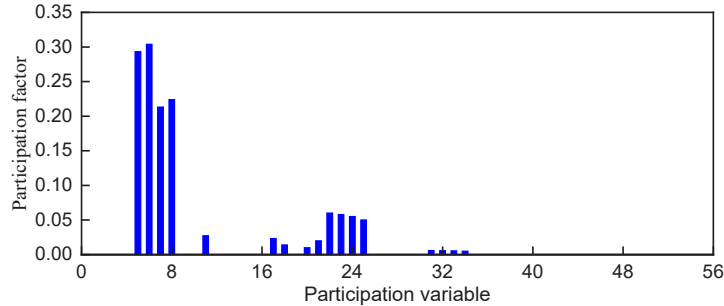


Fig. 5. Participatory factor analysis of SSO-4

Fig. 5 shows that SSO-4 is mainly affected by the interaction between the DFIG magnetic link, RSC inner loop controller, VSC1 controller, and the PLL of VSC1.

### 3.2. Sensitivity analysis of controller parameters

The sensitivity analysis of the control parameters of SSO-4 is shown in Table 3.

Table 3. Eigenvalue sensitivity of SSO-4

Parameters	Eigenvalue sensitivity	Parameters	Eigenvalue sensitivity
$K_{P2}$	$0.0753 + j0.0510$	$K_{PI1}$	$-5.1052 - j0.3878$
$K_{I2}$	$0.0043 + j0.0017$	$K_{II1}$	$0.0036 + j0.0352$
$K_{PO1}$	$-5.1195 - j0.5198$	$K_{PPLL\ VSC1}$	$-0.0566 - j0.0821$
$K_{IO1}$	$0.0027 + j0.0353$	$K_{IPLL\ VSC1}$	$-0.0109 + j0.0074$

Table 3 shows that the sensitivity of the proportional gains of the RSC inner loop, VSC1 outer loop and inner loop controllers, and the PLL to SSO is greater than the integral gains. Therefore, the influence of proportional gains of the controllers on the SSO characteristics will be analyzed.

### 3.3. Impact of wind turbine operating conditions on SSO

The change of the grid connection distance of the wind power and the wind speed, respectively, as well as their influence on SSO characteristics, is shown in Fig. 6.

Looking at the characteristics of the damping ratio and frequency of the system in Fig. 6, it can be concluded that the damping ratio gradually decreases while the frequency gradually

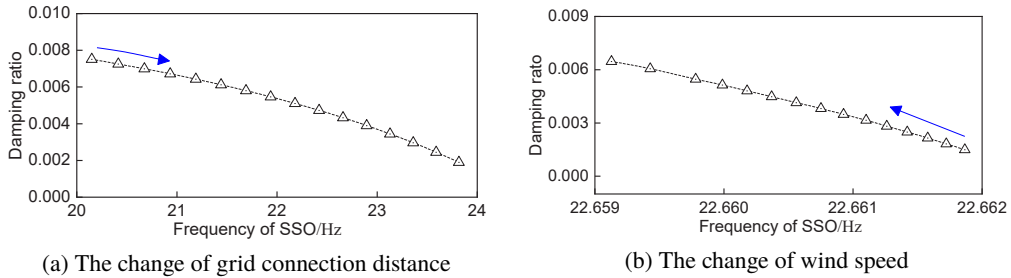


Fig. 6. Changes in locus of damping ratio over oscillation frequency as operating conditions change: (a) grid connection distance; (b) wind speed

increases with the increase of the grid connection distance. Thence, there may be a risk of SSO in the system when the grid connection distance is long. Fig. 6(b) shows that the damping ratio increases while the frequency decreases with the increase of wind speed. However, the influence on frequency is smaller than the damping ratio. Thence, the system would be more stable when wind speed increases.

### 3.4. Impact of controller parameters on SSO

The impact of  $K_{P2}$ ,  $K_{PO1}$ ,  $K_{PI1}$  and  $K_{PPLL VSC1}$  on SSO characteristics is analyzed in this part. Change the corresponding proportionality coefficient and keep other parameters unchanged..

Fig. 7(a) shows that the damping ratio gradually decreases while the frequency increases with the increase of  $K_{P2}$ . Therefore, the stability of the system decreases as  $K_{P2}$  increases. Fig. 7(b)

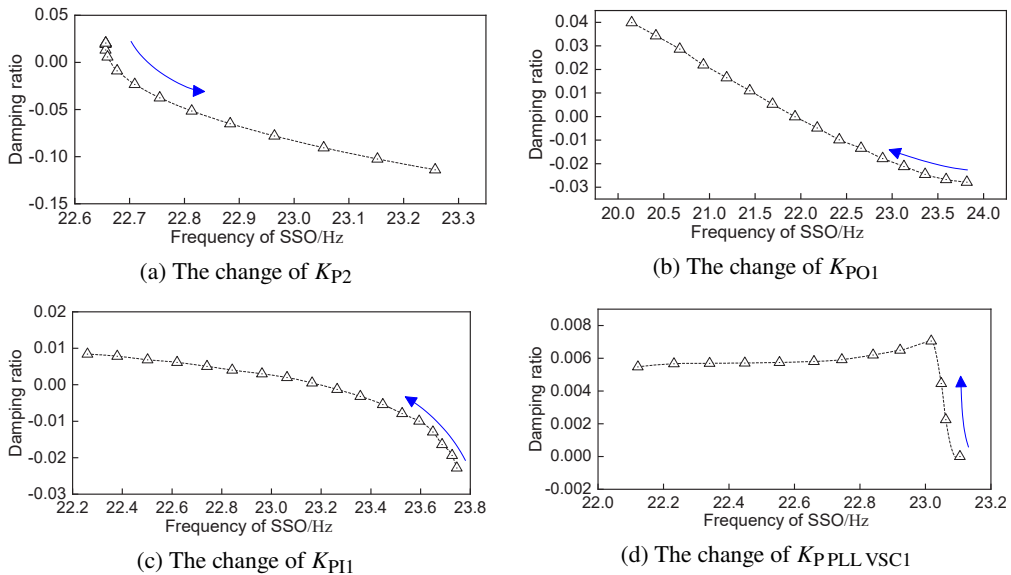


Fig. 7. Changes in the locus of damping ratio over oscillation frequency with the change of parameter controllers: (a) $K_{P2}$ ; (b) $K_{PO1}$ ; (c)  $K_{PI1}$ ; (d)  $K_{PPLL VSC1}$

shows that the damping ratio gradually increases while the frequency gradually decreases with the increase of  $K_{PO1}$ . Therefore, the stability of the system increases as  $K_{PO1}$  increases. As shown in Fig. 7(c), the change trend of the damping ratio and frequency is similar with  $K_{PO1}$ . Therefore, the system is more stable when  $K_{PI1}$  increases. As shown in Fig. 7(d), both the damping ratio and the frequency decrease when  $K_{PPLL\ VSC1}$  increases, thence the stability of the system is decreased when  $K_{PPLL\ VSC1}$  increases. In summary, it can be seen from Fig. 8 that the influence of  $K_{PO1}$  and  $K_{PI1}$  on the damping characteristic is similar, and  $K_{PO1}$  has the greatest influence on the damping ratio and frequency. The PLL has the lowest influence on the SSO characteristic.

## 4. Design of damping controller

### 4.1. Suppression principle of damping controller

When the phase of the electromagnetic torque change  $\Delta T_e$  of the generator lags behind the speed offset  $\Delta\omega$  between  $90^\circ \sim 270^\circ$ , SSO may occur [25]. Then, if the additional electromagnetic torque  $\Delta T'_e$  can be provided in the 1st quadrant, so that the phasor sum  $\Delta T''_e$  of  $\Delta T_e$  and  $\Delta T'_e$  are in the 1st quadrant, the system damping torque is positive and SSO can be suppressed.

### 4.2. Structure of SSDC

A multi-channel variable-parameter SSDC, which is suitable for a DFIG-based wind farm integrated into the grid via the VSC-MTDC system, is designed according to the design method of the multi-channel variable-parameter [26], and the structure of which is shown in Fig. 8.

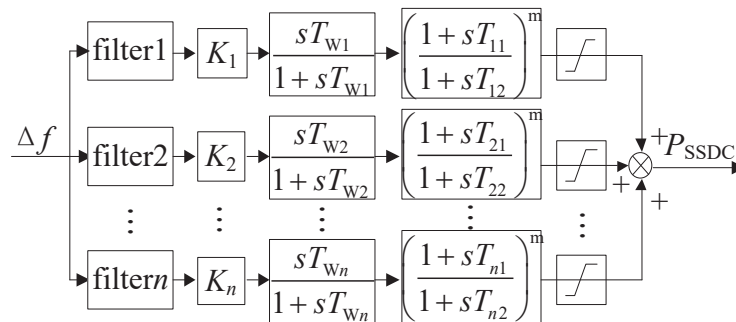


Fig. 8. Structure diagram of multi-channel SSDC

In order to reduce the mutual influence between the phase compensation links as much as possible, a band-pass filter can be used to separate the components. The internal parameters of the SSDC designed based on this method can be adjusted in real time as the operating conditions change. Select the AC voltage of VSC1 AC bus as the input of the SSDC, and the system frequency deviation  $\Delta f$  can be obtained via the measurement link and the PLL. Then, the SSDC output signal can be obtained via DC blocking link, gain, phase compensation, and limiting steps. For the VSC-HVDC system, the inner-loop superposition method is not affected by the control mode

change of the outer-loop controller, and is highly versatile. Thence, the SSDC output signal is superimposed on the  $d$ -axis current reference value  $i_{d\text{ref}}$ , and its additional position is shown in Fig. 9.

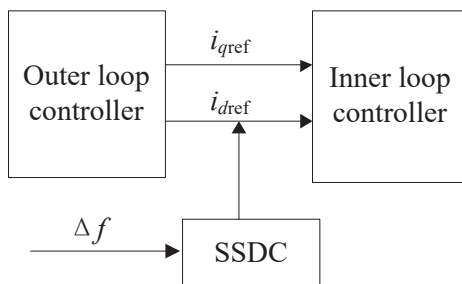


Fig. 9. Signal overlay block diagram of SSDC

In order to minimize the impact of the DC blocking link on the phase compensation: set the time constant of the DC blocking link  $T_W = 5$  s; the limiting link is taken as  $\pm 0.1$  pu; the lead/lag time constants  $T_1$  and  $T_2$  of the phase compensation link can be obtained via [26]. Based on the test signal method, the corresponding phase compensation parameters can be obtained when the input active power of VSC1 changes, as shown in Table 4.

Table 4. Phase compensation parameters

$f$ / Hz	$P = 0.65$ pu		$P = 0.75$ pu		$P = 0.85$ pu	
	$T_1$	$T_2$	$T_1$	$T_2$	$T_1$	$T_2$
2.22	0.107186	0.047951	0.104527	0.049171	0.101868	0.050391
3.27	0.068233	0.034718	0.066413	0.035669	0.064593	0.036621
3.56	0.06169	0.032399	0.060029	0.033295	0.058369	0.034191
3.62	0.060187	0.032116	0.058578	0.032998	0.05697	0.03388
11.01	0.019189	0.01089	0.020162	0.010364	0.021135	0.009839
22.66	0.013342	0.003697	0.013636	0.003618	0.013929	0.003538
27.39	0.008536	0.003955	0.01149	0.002939	0.014444	0.001922
27.7	0.008255	0.003999	0.010986	0.003005	0.013717	0.002011
29.97	0.008063	0.003498	0.009644	0.002924	0.011226	0.002351
34.54	0.005795	0.003664	0.005149	0.004124	0.004502	0.004584
49.97	0.006566	0.001545	0.006584	0.001541	0.006601	0.001537

It can be seen from Table 4 that within the range of VSC1 input active power, the phase lag characteristic changes substantially linearly with input active power. Because the phase lag angle does not change drastically with power,  $T_1$  and  $T_2$  also change approximately linearly within the

change range of power. For example,  $T_1$  and  $T_2$  change as following at 2.22 Hz.

$$T_1 = 0.1244695 - 0.02659P, \quad (17)$$

$$T_2 = 0.040021 + 0.0122P, \quad (18)$$

where  $P$  is the input active power of VSC1.

In the same way, the linear expression of  $T_1$  and  $T_2$  varying with  $P$  at each frequency can be obtained. When transmission line losses are ignored, the input power of VSC1 can reflect the dynamic change of output power of a wind farm. When the participation factors of a certain oscillation mode in the system change so that the output active power of the wind farm will also change, the SSDC can adjust  $T_1$  and  $T_2$  according to the change of the output active power of the wind farm, so that it can make the best damping compensation for the system.

## 5. Simulation verification

### 5.1. Impact of wind farm operating conditions

The impact of a grid connection distance and wind speed on SSO is analyzed in this part.

The results obtained from Fig. 10(a) indicate that the system reaches the critical oscillation point when the grid-connected distance is 7 km, with the increase of the grid-connected distance, the system power oscillation diverges. Fig. 10(b) shows that the system reaches the critical oscillation point when the wind speed is 8.5 m/s. When the wind speed increases from 7.5 m/s to 9.5 m/s, the system power oscillation converges..

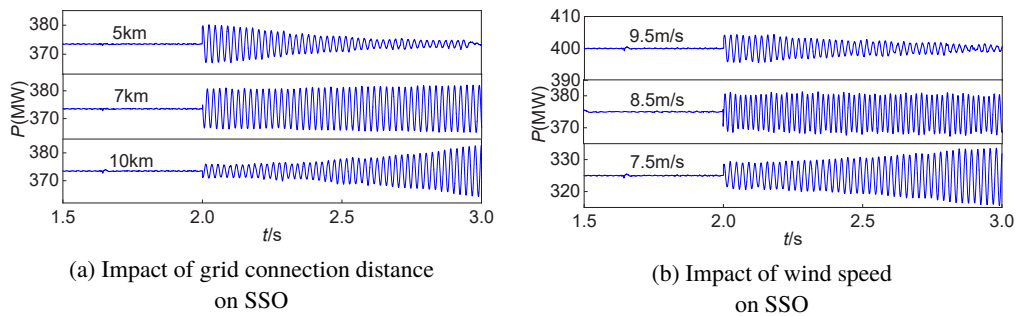


Fig. 10. Impact of wind farm operating conditions: (a) grid connection distance; (b) wind speed

### 5.2. Impact of controller parameters

The operating conditions are as follows: the grid connection distance is set to 5 km, the wind speed is set to 8.5 m/s, the rotating speed is set to 0.8 pu.

According to Fig. 11(a), the system reaches the critical oscillation point when  $K_{P2}$  is about 0.25. When  $K_{P2}$  decreases from 0.25 to 0.18, the system power oscillation converges. According to Fig. 11(b), the system reaches the critical oscillation point when  $K_{P01}$  is about 0.74. When  $K_{P01}$  increases from 0.7 to 0.78, the system power oscillation converges. Fig. 11(c) shows that

the critical value of  $K_{PI1}$  is about 0.44, with the increase of  $K_{PI1}$ , the system power oscillation converges. Fig. 11(d) shows that the critical value of  $K_{P_{PLL\_VSC1}}$  is about 2, with the decrease of  $K_{P_{PLL\_VSC1}}$ , the system power oscillation converges.

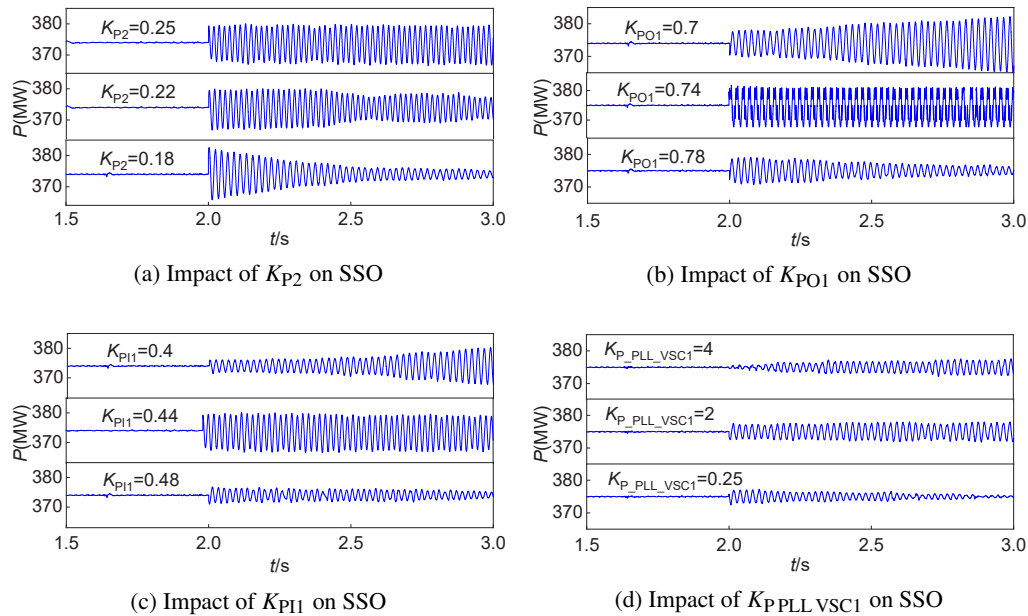


Fig. 11. Impact of controller parameters: (a)  $K_{P2}$ ; (b)  $K_{PO1}$ ; (c)  $K_{PI1}$ ; (d)  $K_{P_{PLL\_VSC1}}$

### 5.3. Verification of multi-channel variable-parameter SSDC effectiveness

Keep other operating conditions unchanged and study the dynamic response of the wind farm output active power when the wind speed is 8.5 m/s and 7.5 m/s.

It can be seen from Fig. 12 that when the wind farm output power changes, the wind farm output active power can stabilize in a short time, which reduces the risk of SSO in the system and indicates the multi-channel variable-parameter SSDC can suppress SSO to a certain extent.

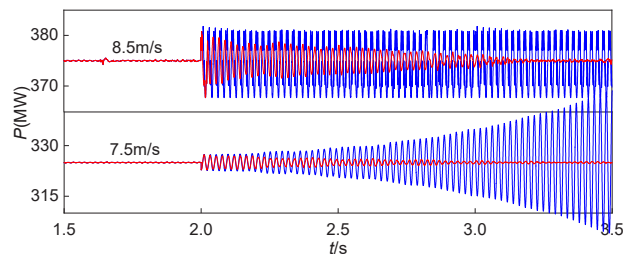


Fig. 12. Output power of wind farm when SSDC is turned on at different wind speeds

## 6. Conclusions

The paper establishes a small-signal model of the system, and analyzes the SSO characteristics of the system based on the eigenvalue analysis method and time-domain simulation. The following conclusions are obtained: 1) When a DFIG-based wind farm is connected via the VSC-MTDC system, the risk of SSO will exist in the system due to the interaction of DFIG and VSC-MTDC system controllers, and the interaction of VSCs; 2) The longer the distance of a wind farm connected to the grid, the lower the wind speed, the higher the risk of SSO in the system; 3) The parameters of controllers such as the proportion gains of the RSC inner loop, the inner and the outer loops of VSC1 and the PLL of VSC1 are more sensitive to SSO than corresponding integration gains; 4) The multi-channel variable-parameter SSDC can increase the damping of each oscillation mode to suppress SSO and avoid the danger of SSO divergence. Besides, it still has a good oscillation suppression effect via adjusting control parameters automatically when the operating conditions of the system change.

## Acknowledgements

This work was supported in part by the Key Research and Development Project of Gansu Province under Grant 18YF1GA056, and in part by the Tianyou innovation team of Lanzhou Jiaotong University under Grant TY202009.

## Appendix

The small signal model of the DFIG is as follows:

$$\Delta \dot{\mathbf{x}}_{\text{DFIG}} = \mathbf{A}_{\text{DFIG}} \Delta \mathbf{x}_{\text{DFIG}} + \mathbf{B}_{\text{DFIG}} \Delta \mathbf{u}.$$

The matrix  $\mathbf{A}_{\text{DFIG}}$  is expressed as follows:

$$\mathbf{A}_{\text{DFIG}} = \begin{bmatrix} \mathbf{A}_m & \mathbf{k}_{m1} \mathbf{k}_{m2} & \mathbf{0}_{4 \times 1} & \mathbf{0}_{4 \times 4} & \mathbf{0}_{4 \times 3} \\ \mathbf{k}_{G3} \mathbf{C}_m & \mathbf{A}_G & \mathbf{0}_{3 \times 1} & \mathbf{k}_{G2} \mathbf{C}_r & \mathbf{0}_{4 \times 3} \\ \mathbf{0}_{1 \times 4} & \mathbf{k}_{DC5} \mathbf{k}_{CG1} & \mathbf{0}_{1 \times 1} & \mathbf{k}_{DC4} \mathbf{C}_r & \mathbf{k}_{DC2} \mathbf{k}_{DC3} + \mathbf{k}_{DC1} \mathbf{C}_g \\ \mathbf{k}_{r1} \mathbf{C}_m & \mathbf{k}_{r2} \mathbf{k}_{CG2} & \mathbf{0}_{4 \times 1} & \mathbf{A}_r & \mathbf{0}_{4 \times 3} \\ \mathbf{0}_{3 \times 4} & \mathbf{0}_{3 \times 4} & \mathbf{k}_{g1} & \mathbf{0}_{3 \times 4} & \mathbf{A}_g + \mathbf{k}_{g2} \mathbf{C}_g \end{bmatrix},$$

where:

$$\mathbf{A}_m = \begin{bmatrix} -\frac{B_s}{2H_g} & \frac{B_s}{2H_g} & 0 & \frac{K_s}{2H_g} \\ \frac{B_s}{2H_t} & -\frac{B_s}{2H_t} & 0 & -\frac{K_s}{2H_t} \\ 1 & 0 & 0 & 0 \\ -1 & 1 & 0 & 0 \end{bmatrix},$$

$$\begin{aligned}
 \mathbf{k}_{m1} &= \begin{bmatrix} \frac{1}{2H_g} \\ 0 \\ 0 \\ 0 \end{bmatrix}, \quad \mathbf{k}_{m2} = \begin{bmatrix} 0 \\ \frac{1}{2H_t} \\ 0 \\ 0 \end{bmatrix}, \quad \mathbf{k}_{G2} = \begin{bmatrix} 0 & 0 \\ 0 & 0 \\ \omega_b & 0 \\ 0 & \omega_b \end{bmatrix}, \quad \mathbf{k}_{g3} = \begin{bmatrix} 0 \\ 0 \\ \omega_s \omega_b \psi_{dr0} \\ -\omega_s \omega_b \psi_{qr0} \end{bmatrix}, \\
 \mathbf{C}_m &= \begin{bmatrix} 1 & 0 & 0 & 0 \end{bmatrix}, \quad \mathbf{C}_r = \begin{bmatrix} K_{P2} & K_{I1} & K_{I2} & 0 & 0 \\ 0 & 0 & K_{P2} & K_{I3} & K_{I2} \end{bmatrix}, \\
 \mathbf{k}_{DC1} &= [i_{qgo} \ i_{dgo}], \quad \mathbf{k}_{DC2} = [u_{qgo} \ u_{dgo}], \quad \mathbf{k}_{DC4} = [-i_{qro} \ -i_{dro}], \\
 \mathbf{k}_{DC3} &= \begin{bmatrix} 0 & -\frac{1}{\omega_s L_g} \\ \frac{1}{\omega_s L_g} & 0 \end{bmatrix}, \quad \mathbf{k}_{DC5} = [-u_{qro} \ -u_{dro}], \\
 \mathbf{C}_g &= \begin{bmatrix} K_{Pg1} & K_{Idg} & K_{Ig1} & 0 \\ 0 & 0 & K_{Ig2} & 0 \end{bmatrix}, \quad \mathbf{k}_{g2} = \begin{bmatrix} 0 \\ K_{P1} \\ 0 \\ 0 \end{bmatrix}, \\
 \mathbf{k}_{g1} &= \begin{bmatrix} -1 \\ -K_{Pdf} \\ 0 \end{bmatrix}, \quad \mathbf{k}_{r2} = \begin{bmatrix} -u_{ds0} & -u_{qs0} & 0 & 0 \\ -K_{P1}u_{ds0} & -K_{P1}u_{qs0} & 0 & -1 \\ -u_{qs0} & u_{ds0} & 0 & 0 \\ -K_{P3}u_{qs0} & K_{P3}u_{ds0} & -1 & 0 \end{bmatrix}, \quad \mathbf{k}_{g2} = \begin{bmatrix} 0 & 0 \\ -1 & 0 \\ 0 & -1 \end{bmatrix}, \\
 \mathbf{A}_g &= \begin{bmatrix} 0 & 0 & 0 \\ K_{Idg} & 0 & 0 \\ 0 & 0 & 0 \end{bmatrix}, \quad \mathbf{A}_g = \begin{bmatrix} 0 & 0 & 0 & 0 \\ K_{I1} & 0 & 0 & 0 \\ 0 & 0 & K_{I3} & 0 \\ 0 & 0 & 0 & 0 \end{bmatrix}, \\
 \mathbf{k}_{CG2} &= \begin{bmatrix} \frac{X_{rr}}{D} & 0 & -\frac{X_m}{D} & 0 \\ 0 & \frac{X_{rr}}{D} & 0 & -\frac{X_m}{D} \\ -\frac{X_m}{D} & 0 & \frac{1}{X_r + X_m} \left(1 + \frac{X_m^2}{D}\right) & 0 \\ 0 & -\frac{X_m}{D} & 0 & \frac{1}{X_r + X_m} \left(1 + \frac{X_m^2}{D}\right) \end{bmatrix}, \\
 \mathbf{A}_G &= \begin{bmatrix} -\frac{\omega_b R_s X_{rr}}{D} & -\omega_s \omega_b & -\frac{\omega_b R_s X_m}{D} & 0 \\ \omega_s \omega_b & \frac{\omega_b R_s X_{rr}}{D} & 0 & \frac{\omega_b R_s X_m}{D} \\ \frac{\omega_b R_r X_m}{D} & 0 & \frac{\omega_b R_r X_{ss}}{D} & -s_0 \omega_s \omega_b \\ 0 & \frac{\omega_b R_r X_m}{D} & -s_0 \omega_s \omega_b & \frac{\omega_b R_r X_{ss}}{D} \end{bmatrix}.
 \end{aligned}$$

The small signal model of VSC1 is as follows:

$$\Delta \dot{\mathbf{x}}_{con1} = \mathbf{A}_{con1} \Delta \mathbf{x}_{con1} + \mathbf{B}_{con1} \Delta \mathbf{u}_{con1}.$$

The matrix  $A_{\text{con1}}$  is expressed as follows:

$$A_{\text{con1}} = \begin{bmatrix} A_{\text{ac}} & B_C k_{\text{uc udc}} & B_C k_{\text{uc } \theta} C_{\text{pll}} & B_C k_{\text{uc Mdg}} C_C \\ k_{\text{idc Idq}} & \mathbf{0}_{1 \times 1} & k_{\text{udc } \theta} C_{\text{pll}} & k_{\text{udc Mdg}} C_C \\ B_{\text{pll}} k_{\varphi \text{Idq}} & B_{\text{pll}} k_{\varphi \text{udc}} & A_{\text{pll}} + B_{\text{pll}} k_{\varphi \theta} C_{\text{pll}} & B_{\text{pll}} k_{\varphi \text{Mgd}} C_C \\ B_{\text{cfl}} k_{\text{fil Idq}} & B_{\text{cfl}} k_{\text{fil udc}} & B_{\text{cfl}} k_{\text{fil } \theta} C_{\text{pll}} & A_c + B_{\text{cfl}} k_{\text{fil Mdg}} C_C \end{bmatrix},$$

where:

$$A_{\text{ac}} = \begin{bmatrix} -\frac{R_{\text{tot}}}{L_{\text{tot}}} & \omega \\ \omega & -\frac{R_{\text{tot}}}{L_{\text{tot}}} \end{bmatrix}, \quad A_{\text{pll}} = \begin{bmatrix} 0 & -K_{\text{Ipll}} \\ 1 & -K_{\text{Ppll}} \end{bmatrix}, \quad A_c = \begin{bmatrix} 0 & 0 & 0 & 0 \\ K_{\text{IO}} & 0 & 0 & 0 \\ 0 & 0 & 0 & 0 \\ 0 & 0 & K_{\text{IO}} & 0 \end{bmatrix},$$

$$B_{\text{pll}} = \begin{bmatrix} K_{\text{Ipll}} \\ K_{\text{Ppll}} \end{bmatrix}, \quad C_{\text{pll}} = [0 \quad 1],$$

$$B_{\text{ref}} = \begin{bmatrix} 0 & 0 & 0 & 0 & 0 \\ 0 & 0 & K_{\text{PO}} & 0 & 0 \\ 0 & 0 & 0 & 0 & 0 \\ 0 & 0 & 0 & 0 & -K_{\text{PO}} \end{bmatrix}, \quad B_{\text{cfl}} = -B_{\text{ref}} \begin{bmatrix} 0 & 0 \\ 0 & 0 \\ -1 & 0 \\ 0 & -1 \end{bmatrix},$$

$$k_{\text{uc udc}} = \begin{bmatrix} M_{d0} \\ M_{q0} \end{bmatrix}, \quad k_{\text{uc } \theta} = \frac{K_t u_{\text{dc}0}}{2} \begin{bmatrix} M_{d0} \\ M_{q0} \end{bmatrix}, \quad k_{\text{uc Mdg}} = \frac{K_t u_{\text{dc}0}}{2},$$

$$k_{\text{idc Idq}} = \frac{3K_t}{4C_{\text{dc}}} \begin{bmatrix} M_{d0} & M_{q0} \end{bmatrix},$$

$$k_{\text{udc } \theta} = \frac{3K_t}{4C_{\text{dc}}} \begin{bmatrix} I_{d0} & I_{q0} \end{bmatrix} \begin{bmatrix} M_{d0} \\ M_{q0} \end{bmatrix}, \quad k_{\text{uc Mdg}} = \frac{3K_t}{4C_{\text{dc}}} \begin{bmatrix} I_{d0} & I_{q0} \end{bmatrix},$$

$$k_{\varphi \text{Idq}} = \begin{bmatrix} \frac{R u_{\text{pq}0}}{u_{\text{pd}0}^2 \left[ 1 + \left( \frac{u_{\text{pq}0}}{u_{\text{pd}0}} \right)^2 \right]} & \frac{R u_{\text{pd}0}}{u_{\text{pd}0}^2 \left[ 1 + \left( \frac{u_{\text{pq}0}}{u_{\text{pd}0}} \right)^2 \right]} \end{bmatrix},$$

$$k_{\varphi \text{udc}} = \begin{bmatrix} \frac{L_1 u_{\text{pq}0}}{u_{\text{pd}0}^2 \left[ 1 + \left( \frac{u_{\text{pq}0}}{u_{\text{pd}0}} \right)^2 \right]} & \frac{L_1 u_{\text{pd}0}}{u_{\text{pd}0}^2 \left[ 1 + \left( \frac{u_{\text{pq}0}}{u_{\text{pd}0}} \right)^2 \right]} \end{bmatrix} k_{\text{uc udc}}, \quad B_c = \begin{bmatrix} -\frac{1}{L_{\text{tot}}} \\ \frac{1}{L_{\text{tot}}} \end{bmatrix},$$

$$C_c = \begin{bmatrix} -K_{\text{PI}} K_{\text{IO}} & -K_{\text{II}} & 0 & 0 \\ 0 & 0 & -K_{\text{PI}} K_{\text{IO}} & K_{\text{II}} \end{bmatrix},$$

$$k_{\varphi \text{Mdg}} = \begin{bmatrix} \frac{L_1 u_{\text{pq}0}}{u_{\text{pd}0}^2 \left[ 1 + \left( \frac{u_{\text{pq}0}}{u_{\text{pd}0}} \right)^2 \right]} & \frac{L_1 u_{\text{pd}0}}{u_{\text{pd}0}^2 \left[ 1 + \left( \frac{u_{\text{pq}0}}{u_{\text{pd}0}} \right)^2 \right]} \end{bmatrix} k_{\text{uc Mdg}},$$

$$\begin{aligned}
 \mathbf{k}_{fil\ udc} &= \begin{bmatrix} \frac{3}{2} \begin{bmatrix} i_{d0} & i_{q0} \\ -i_{q0} & i_{d0} \end{bmatrix} + \begin{bmatrix} u_{pd0} & u_{pq0} \\ u_{pd0} & -u_{pd0} \end{bmatrix} L_{2pcc} K_{uc\ udc} \\ \mathbf{1}_{2 \times 2} L_{2pcc} K_{uc\ udc} \\ 0 \\ \begin{bmatrix} 0 \\ 0 \end{bmatrix} \end{bmatrix}, \\
 \mathbf{k}_{fil\ Mdq} &= \begin{bmatrix} L_{2pcc} K_{uc\ Mdq} \mathbf{1}_{2 \times 2} \frac{3}{2} \begin{bmatrix} i_{d0} & i_{q0} \\ -i_{q0} & i_{d0} \end{bmatrix} + \begin{bmatrix} u_{pd0} & u_{pq0} \\ u_{pd0} & -u_{pd0} \end{bmatrix} \\ L_{2pcc} K_{uc\ Mdq} \mathbf{1}_{2 \times 2} \\ \mathbf{0}_{1 \times 2} \\ \mathbf{0}_{2 \times 2} \end{bmatrix}, \\
 \mathbf{k}_{fil\ \theta} &= \begin{bmatrix} i_{d0} + i_{q0} \\ i_{d0} + i_{q0} \end{bmatrix}.
 \end{aligned}$$

Therefore, the small signal model of the VSC-MTDC can be obtained in the same way. Then, the small signal model of the whole system can be obtained:

$$\Delta \dot{\mathbf{x}} = \mathbf{A} \Delta \mathbf{x} + \mathbf{B} \Delta \mathbf{u}.$$

The state matrix  $\mathbf{A}$  can be described as follows:

$$\mathbf{A} = \begin{bmatrix} A_{DFIG} & & & & & \mathbf{0} \\ \mathbf{k}_1 & A_{con1} & & & & \mathbf{B}_{line1} \mathbf{H}_{line1} \\ & & A_{con2} & & & \mathbf{B}_{line2} \mathbf{H}_{line2} \\ & & & A_{con3} & & \mathbf{B}_{line3} \mathbf{H}_{line3} \\ & & & & A_{con4} & \mathbf{B}_{line4} \mathbf{H}_{line4} \\ \mathbf{0} & \mathbf{B}_{net1} \mathbf{H}_{dc1} & \mathbf{B}_{net2} \mathbf{H}_{dc2} & \mathbf{B}_{net3} \mathbf{H}_{dc3} & \mathbf{B}_{net4} \mathbf{H}_{dc4} & \mathbf{A}_{net} \end{bmatrix},$$

where:

$$\mathbf{A}_{net} = \begin{bmatrix} -\frac{R_{21}}{L_{21}} & & & & \\ & -\frac{R_{31}}{L_{31}} & & & \\ & & -\frac{R_{42}}{L_{42}} & & \\ & & & -\frac{R_{43}}{L_{43}} & \\ & & & & \end{bmatrix},$$

$$\mathbf{B}_{net1} = \begin{bmatrix} -\frac{1}{2L_{21}} \\ 0 \\ 0 \\ 0 \end{bmatrix}, \quad \mathbf{B}_{net2} = \begin{bmatrix} 0 \\ -\frac{1}{2L_{31}} \\ 0 \\ 0 \end{bmatrix}, \quad \mathbf{B}_{net3} = \begin{bmatrix} 0 \\ 0 \\ -\frac{1}{2L_{42}} \\ 0 \end{bmatrix}, \quad \mathbf{B}_{net4} = \begin{bmatrix} 0 \\ 0 \\ 0 \\ -\frac{R_{43}}{L_{43}} \end{bmatrix},$$

$$\mathbf{B}_{linei} = \begin{bmatrix} 0 & -\frac{1}{C_{dci}} & 0 & 0 \end{bmatrix}^T, \quad \mathbf{k}_1 = \begin{bmatrix} \mathbf{0}_{2 \times 4} & \mathbf{C}_{CG1} & \mathbf{0}_{2 \times 8} \\ & \mathbf{0}_{9 \times 16} & \end{bmatrix},$$

$$C_{CG1} = \begin{bmatrix} 0 & \frac{X_{rr}}{X_s X_r + (X_s + X_r) X_m} & 0 & \frac{-X_m}{X_s X_r + (s + X_r) X_m} \\ \frac{X_{rr}}{X_s X_r + (X_s + X_r) X_m} & 0 & \frac{-X_m}{X_s X_r + (X_s + X_r) X_m} & 0 \end{bmatrix},$$

where:  $R_{ij}$  and  $L_{ij}$  represent the resistance and inductance of a DC transmission line,  $i$  represents the different converters. Each element of  $H_{linei}$  has two values of 0 and 1, when  $\Delta x_{net}(j)$  is the input current of the DC transmission line, which is connected with the  $i$ -th converter,  $H_{linei}(i, j) = 1$ .

Table 5. Main parameters of the system

Parameters	Value	Parameters	Value
Rated stator/rotor current	0.8511 pu./0.8968 pu	Stator/rotor winding resistance	0.0084pu/0.0083 pu
Stator/rotor leakage inductance	0.167 pu/0.1323 pu	Magnetizing inductance	5.419 pu
$L_1$	0.06278 H	$K_{P1}/K_{I1}/K_{P2}/K_{I2}/K_{P3}/K_{I3}$	0.4/10/0.02/0.2/0.3/10
$K_{Pdg}/K_{Idg}/K_{Pg}/K_{Ilg}$	10/2/0.1/2	$K_{PI2}/K_{II2}/K_{PO2}/K_{IO2}$	0.3/10/0.2/10
$K_{PI3}/K_{II3}/K_{PO3}/K_{IO3}$	8/10/6/10	$K_{PI4}/K_{II4}/K_{PO4}/K_{IO4}$	0.35/10/0.4/10

## References

- [1] Tang G.F., *HVDC based on voltage source converter*, China Electric Power Press (2010).
- [2] Li C.S., Li Y.K., Guo J., He P., *Research on emergency DC power support coordinated control for hybrid multi-infeed HVDC system*, Archives of Electrical Engineering, vol. 61, no. 1, pp. 5–21 (2020).
- [3] Liu T.Q., Tao Y., Li B.H., *Critical problems of wind farm integration via MMC-MTDC system*, Power System Technology, vol. 41, no. 10, pp. 3251–3260 (2017).
- [4] Wu J.H., Ai Q., *Research on multi-terminal VSC-HVDC system for wind-farms*, Power System Technology, vol. 33, no. 4, pp. 22–27 (2009).
- [5] Chen C., Du W.J., Wang H.F., *Review on mechanism of sub-synchronous oscillations caused by grid-connected wind farms in power systems*, Southern Power System Technology, vol. 12, no. 1, pp. 84–93 (2018).
- [6] Amin M., Molinas M., *Understanding the origin of oscillatory phenomena observed between wind farms and HVDC systems*, IEEE Journal of Emerging and Selected Topics in Power Electronics, vol. 5, no. 1, pp. 378–392 (2017).
- [7] Wang W.S., Zhang C., He G.Q., Li G.H., Zhang J.Y., Wang H.J., *Overview of research on subsynchronous oscillations in large-scale wind farm integrated system*, Power System Technology, vol. 41, no. 4, pp. 1050–1060 (2017).
- [8] Jiang Q.R., Wang L., Xie X.R., *Study on oscillations of power-electronized power system and their mitigation schemes*, High Voltage Engineering, vol. 43, no. 4, pp. 1057–1066 (2017).
- [9] Xie X.R., Liu H.K., He J.B., Liu H., Liu W., *On new oscillation issues of power system*, Proceedings of the CSEE, vol. 38, no. 10, pp. 2821–2828+3133 (2018).

- [10] Wang L., Yang Z.H., Lu X.Y., Prokhorow A.V., *Stability analysis of a hybrid multi-infeed HVDC system connected between two offshore wind farms and two power grids*, IEEE Transactions on Industry Applications, vol. 53, no. 3, pp. 1824–1833 (2017).
- [11] Kunjumammed L.P., Pal B.C., Oates C., Dyke K.J., *Electrical oscillations in wind farm systems: analysis and insight based on detailed modeling*, IEEE Transactions on Sustainable Energy, vol. 7, no. 1, pp. 51–61 (2016).
- [12] Sun K., Yao W., Wen J.Y., *Mechanism and characteristics analysis of subsynchronous oscillation caused by DFIG-based wind farm integrated into grid through VSC-HVDC system*, Proceedings of the CSEE, vol. 38, no. 22, pp. 6520–6533 (2018).
- [13] Song S.H., Zhao S.Q., *Analysis of sub-synchronous oscillation of DFIG-based Wind Farm integrated to grid through VSC-HVDC system based on torque method*, Power System Technology, vol. 44, no. 2, pp. 630–636 (2020).
- [14] Bian X.Y., Ding Y., Mai K., Zhou Q., Zhao Y., Tang L., *Sub-Synchronous oscillation caused by grid-connection of offshore wind farm through VSC-HVDC and its mitigation*, Automation of Electric Power Systems, vol. 42, no. 17, pp. 25–39 (2018).
- [15] Lyu J., Dong P., Shi G., Cai X., Li X.L., *Subsynchronous oscillation and its mitigation of MMC-based HVDC with large doubly-fed induction generator-based wind farm integration*, Proceedings of the CSEE, vol. 35, no. 19, pp. 4852–4860 (2015).
- [16] Lyu J., Cai X., Amin M., Molinas M., *Sub-synchronous oscillation mechanism and its suppression in MMC-based HVDC connected wind farms*, IET Generation, Transmission and Distribution, vol. 12, no. 4, pp. 1021–1029 (2018).
- [17] Shao B.B., Zhao S.Q., Pei J.K., Li R., *Subsynchronous oscillation characteristics analysis of grid-connected direct-drive wind farms via VSC-HVDC system*, Power System Technology, vol. 43, no. 9, pp. 3344–3355 (2019).
- [18] Chen B.P., *Study on characteristics and suppression of sub/super-synchronous oscillation caused by power system with D-PMSG and VSC-HVDC*, Wuhan University (2018).
- [19] Guo X.S., Li Y.F., Xie X.T., Hou Y.L., Zhang D., *Sub-synchronous oscillation characteristics caused by PMSG-based wind plant farm integrated via flexible HVDC system*, Proceedings of the CSEE, vol. 40, no. 4, pp. 1149–1160+1407 (2020).
- [20] Sun K., *Mechanism and characteristics analysis of subsynchronous oscillation caused by DFIG-based wind farm integrated into grid through VSC-HVDC system*, Huazhong University of Science and Technology (2018).
- [21] He J., Li Q., Qin S.Y., Wang R.M., *DFIG wind turbine modeling and validation for LVRT behavior*, IEEE PES Innovative Smart Grid Technologies, Tianjin, pp. 1–5 (2012).
- [22] Lu X.J., Lin W.X., Wen J.Y., Li Y.F., Wu Y.L., An T., *Modularized small signal modeling method for DC grid*, Proceedings of the CSEE, vol. 36, no. 11, pp. 2880–2889 (2016).
- [23] Kalcon G.O., Adam G.P., Anaya-Lara O., Lo S., Uhlen K., *Small-signal stability analysis of multi-terminal VSC-based DC transmission systems*, IEEE Transactions on Power Systems, vol. 27, no. 4, pp. 1818–1830 (2012).
- [24] Zhou G.L., Shi X.C., Fu Ch., Wei X.G., Zhu X.R., *VSC-HVDC discrete model and its control strategy under unbalanced input voltage*, Transactions of China Electrotechnical Society, vol. 23, no. 12, pp. 137–143+159 (2008).
- [25] Gao B.F., Zhao C.Y., Xiao X.N., Yin W.Y., Guo C.L., Li Y.N., *Design and implementation of SSDC for HVDC*, High Voltage Engineering, vol. 36, no. 2, pp. 501–506 (2010).
- [26] Jiang P., Hu T., Wu X., *VSC-HVDC multi-channel additional damping control suppresses sub-synchronous oscillation*, Electric Power Automation Equipment, vol. 31, no. 9, pp. 27–31 (2011).